Acta Mech
https://doi.org/10.1007/s00707-023-03670-8

ORIGINAL PAPER

N. D. Karaferis · V. E. Melissianos · D. Vamvatsikos

Mechanical modeling, seismic fragility, and correlation issues for groups of spherical pressure vessels

Received: 10 June 2023 / Revised: 16 July 2023 / Accepted: 18 July 2023
© The Author(s) 2023

Abstract A roadmap is outlined for determining comprehensive seismic fragility curves for (single or groups of) spherical pressure vessel structures commonly found in oil refineries. The developed modeling techniques aim to strike a balance between accuracy and computational efficiency, with a focus on capturing the most pertinent failure modes relevant to these structural types. First, a set of "partial" fragilities is determined based on each vessel's fill ratio, as the response varies substantially depending on the amount of liquid content. Considering that a seismic assessment process invariably involves simultaneous consideration of such partial fragilities, a Monte Carlo-based approach is employed for their combination. The results naturally depend on the level of correlation employed, but can be almost perfectly matched by simpler analytical methods in the edge cases of full and zero correlation.

1 Introduction

Pressure vessels are common structures in oil refineries used for storage of gaseous fuels, such as propane and butane. Safe design is essential for these structures, given their importance; thus, seismic design and construction practices are well-studied subjects in current literature, with many studies and regulations addressing and proposing various design choices and modeling approaches (e.g., [1–5]) or generally examining the performance of these structures (e.g., [6–10]). On the other hand, there are not many studies analyzing pressure vessel structures from a risk assessment standpoint (e.g., [11–13]). After all, accurate prediction of their vulnerability is key for the stakeholders to be able to safeguard them against catastrophic damages, but also to estimate economic losses, determine mitigation strategies, and formulate emergency response plans.

Owing to the above, a typical spherical pressure vessel on braced legs was selected as a case study. While there are already well-established modeling approaches for such typologies, there is a certain and critical disconnect between the mechanical model and the operational reality of refineries. Specifically, analysts tend to consider only the worst-case scenario of a fully filled condition, conservatively neglecting the fact that such vessels are typically filled to different levels within the same facility, while the fill ratio may vary within a single day due to operational reasons, e.g., increased or decreased production, selling of product, etc. The aforementioned conservative consideration is desirable for design, but at the same time it essentially introduces unwanted bias in the assessment. Due to partially filled conditions, seemingly identical structures can undergo disparate levels of seismic damage. This has been observed, for example, in wine storage tanks after the 2013 Seddon and 2016 Kaikura events in New Zealand [14, 15], as well as for liquid storage tanks in the Habbas plant after the 1999 Kocaeli, Türkiye, earthquake. Most tellingly, in the latter case, out of three otherwise identical tanks, two 85%-filled tanks collapsed, while the 25%-filled one survived [16].

N. D. Karaferis (✉) · V. E. Melissianos · D. Vamvatsikos
School of Civil Engineering, National Technical University of Athens, 9 Iroon Polytechneiou Str., Zografou Campus, Zographos, 15772 Athens, Greece
e-mail: nkaraferis@mail.ntua.gr

Published online: 14 August 2023

Fig. 1 Schematic illustration of typical spherical pressure vessels

Accounting for such discrepancies is important for accurately assessing the safety of a critical industrial facility. To do so, the modeling approach of Karamanos [17], as later elaborated by Karamanos et al. [18], Patkas and Karamanos [19], and Drosos et al. [20], is employed. This allows utilizing a reduced-order model to capture the impulsive and convective modes of response, thus incorporating the beneficial effects of a reduced reactive mass and sloshing-induced damping, akin to a nearly tuned mass damper.

The adopted model is able to capture efficiently the most critical failure modes, addressing specific damage states (DS) likely to be encountered, or equivalently limit states (LSs) to be exceeded, at increasing levels of seismic intensity. The seismic demands were assessed in terms of pertinent engineering demand parameters (EDPs) using incremental dynamic analysis (IDA, [21, 22]). This process was followed for several different fill ratios (FR) of the vessels. For each case, analytical seismic fragility curves were computed at the level of a single asset. In turn, a practical framework is proposed for expanding such results to a group of assets, as they typically reside in actual facilities, introducing the fill ratio variability to the assessment process of ensembles of pressure vessels, thus offering a flexible framework to match the operational reality of any facility. It is envisaged that this will better address both the need for uninterrupted refinery operation following the occurrence of an earthquake, along with mitigation action planning.

2 Mechanical model

Spherical pressure vessels are steel structures that are typically placed above ground and supported circumferentially by columns that can be either braced or unbraced. In this case study, only braced vessels are considered. A schematic illustration of a typical group of spherical pressure vessels is presented in Fig. 1, showcasing the structures' geometry and main characteristics. Herein, the vessel characteristics reported by Moschonas et al. [11] are adopted as a case study. The diameter of the sphere is $D = 20.22$m, the average shell thickness is $t_s = 42$ mm, and the height to the equator of the sphere is $H = 13.63$m. The shell is assumed to be thick enough to be able to resist the internal pressure applied to it. The support system consists of 12 columns that are X-braced. The 3.04 m-high bottom part of the columns has a circular hollow section of CHS1100 × 30; this reduces to CHS1100 × 25 in the upper part. The braces are plates with cross section 250 × 35 mm. The total mass of the vessel consists of the steel structure mass (M_{sv}) and the mass of the liquid contained (M_{liq}), which are $M_{sv} = 421550$ kg and $M_{liq} = 2362570$ kg, respectively, if the vessel is filled to its full capacity. The liquid density equals $\rho_{liq} = 553$ kg/m^3 [11].

Regarding the structural model, two alternative approaches are available. First, one may choose to offer a detailed finite element model of the shell structure and its support [6–13], potentially also including a proper discretization of the liquid mass, as well as fluid–structure interaction [23–26]. Such a rigorous model can offer accurate representation of critical parts of the structure, for example, addressing the shell-column joint [27] and the brace–column connection. However, it comes at considerable computational cost.

Alternatively, one may employ a reduced-order model that accounts for the salient characteristics of the structure and its most important failure modes. The first simplification that is nearly universally used is the

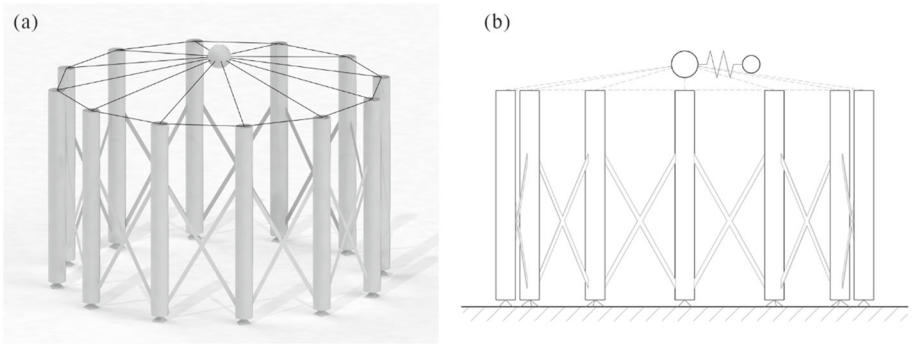

Fig. 2 Reduced-order model of typical spherical pressure vessels: **a** 3D view of the model showing the location of the impulsive and steel structure mass at the center of the vessel, **b** 2D view of the conceptual introduction of the convective mass via translational zero-length element springs

reduction of the fluid mass to its impulsive and convective components [17–20]; thus, the entire fluid is only represented by two point masses being connected with springs. Then, one typically disregards the flexibility of the vessel itself, as any deformation the shell may undergo due to the seismic excitation is insignificant when compared to that of the supporting system. Furthermore, the pressures developing inside the shell are similarly ignored since they do not reduce the strength of the overall structure or the buckling strength of the shell, given that they can even be beneficial in post-buckling behavior [4, 12, 28]. In other words, the shell is not expected to fail before the supporting structure's elements; therefore, one may simply disregard it in the model and directly connect the impulsive and convective masses to the supporting columns. Finally, the columns themselves can be discretized into beam-column elements, while braces can be modeled with truss elements (or multiple beam-column ones) with appropriate force–deformation characteristics [29, 30]. Such reduced-order models can sufficiently address the dominant modes of failure related to the supporting structure of the vessel, as observed in past events [8, 13], and have received attention in pertinent literature (e.g., [4, 9, 11, 12]). Given the substantial number of nonlinear response-history analyses required for a high-fidelity fragility analysis, this will be our modeling method of choice.

The model is developed using the OpenSees analysis platform [31], and its overview is illustrated in Fig. 2a. The supporting columns are pinned at their base, with the connections expected to stay free of damage in even high-intensity seismic events. Each column is represented by three force-based beam-column elements with fiber sections: one for the lower 3.04 m-high part of CHS1100 × 30 section, a second of CHS1100 × 25 section that reaches the upper bracing level at 8.86 m from the ground, and a final part of CHS1100 × 25 section up to the upper end of the column. The length of the latter element should also include part of the transition length where the CHS column merges into the spherical vessel. As proposed by Wieschollek et al. [5] and shown in Fig. 2, this requires lengthening the column elements above the uppermost attachment point of the braces to reach an effective overall length equal to

$$L_c = H - 0.45 \cdot L_s \tag{1}$$

where H is the total height of the column including the entire transition piece (i.e., the height to the equator of the sphere) and L_s is the length of the transition segment itself, from the point where the column starts merging to the shell until the equator point. For the case at hand, the effective overall length of the column is $L_c = 13.63 - 0.45 \cdot 3.29 = 12.15$m.

An elastic-hardening fiber material is employed to model the steel fibers, using 1% hardening ratio. The steel conforms to grade SA 572 Gr. 50 or its equivalent S355 [11], with a mean yield strength at 408.25 MPa, taking, also, into account an overstrength factor of $\gamma_{ov} = 1.15$, as proposed by EN 1998–1:2004 [32]. The actual overstrength for S355 steel grade may depend on the batch and the manufacturer and can range within 1.12–1.45 [33]. P-Δ effects are also considered via a first-order treatment.

The braces are modeled by truss elements with a corotational geometric transformation. The upper bracing point where the braces are connected to the column is at height equal to 8.86 m from the ground level, or around 2/3 of H. Due to their thin profile, the plate sections have essentially no compression strength; as soon as any compression is applied they are expected to buckle. In tension, they are modeled by an elastic-hardening material conforming to SA 738 Gr. B [11] with hardening ratio of 1% and nominal yielding strength of 415 MPa (e.g., [34]); the mean yield strength is again calculated by applying the overstrength factor $\gamma_{ov} = 1.15$ to reach

Table 1 Spherical pressure vessel's mass properties and eigenperiods for varying fill ratios

FR	M_{tot}(kg)	M_I(kg)†	M_C(kg)†	T_{tot}(s)	T_I(s)	T_C(s)
0.95	2,665,990	2,162,520 (96%)	81,920 (04%)	0.66	0.65	2.66
0.85	2,429,740	1,691,090 (84%)	317,090 (16%)	0.63	0.59	3.50
0.75	2,193,480	1,264,800 (71%)	507,130 (29%)	0.60	0.53	4.11
0.65	1,957,220	906,200 (59%)	629,470 (41%)	0.57	0.47	4.56
0.55	1,720,970	617,610 (48%)	681,800 (52%)	0.53	0.41	4.93
0.45	1,484,710	393,580 (37%)	669,580 (63%)	0.50	0.37	5.25
0.35	1,248,450	226,980 (27%)	599,920 (73%)	0.45	0.33	5.54

† Percentage relative to the mass of the liquid in the vessel ($FR{\cdot}M_{liq}$)

477.25 MPa. For such slender brace sections undergoing cyclic deformation, premature brace fracture can be expected due to low-cycle fatigue and the potential accumulation of local deformations. Sen et al. [35] proposed employing a drift range of 1.50% to signal fracture for a 45° inclined brace. This translates to an ultimate tensile strain of $\varepsilon_u = 0.67\%$ in our case study, assuming that the entirety of the proposed drift range applies in tension to account for the minimal development of compression in ultra-slender braces.

Then, regarding the modeling of the mass, for a fill ratio of $FR = 1$ (fully filled condition), one can faithfully capture the structural response by concentrating the full mass of the structure and the liquid at the center of the sphere (see [18]). For $FR < 1$, the total mass (M_{tot}) of the structure becomes

$$M_{tot} = M_{sv} + FR \cdot M_{liq} \tag{2}$$

If a similar modeling approach was followed as for $FR = 1$, one could estimate a single "total" eigenperiod, T_{tot}, which would decrease with decreasing FR, but would be otherwise fictional, as it would disregard the hydrodynamic behavior of the liquid. Instead, the effect of the latter is taken into account following the approach of Housner [36] to model the hydrodynamic effects as the combination of two modes: an impulsive mode, where the liquid moves in unison with the vessel, and a convective mode, which represents the (first mode of) liquid sloshing. For simplicity, higher sloshing modes are disregarded, since their contribution to the overall response of the vessel is insignificant. Owing to the above rationale, the liquid mass is divided into two discrete masses (Fig. 2b), namely the impulsive mass (M_I) and the convective mass (M_C). Their relative ratio depends on the fill ratio of the vessel [17–20], as shown in Table 1.

The impulsive mass is placed at the center of the spherical vessel and rigidly connected to the supporting columns, where the vessel itself effectively generates a horizontal diaphragm action, forcing all columns to displace in unison. The convective mass is connected to the impulsive one via translational zero-length springs in both principal axes, having stiffness that is calculated to reproduce the (first) convective angular frequency, ω_C [20]:

$$K_C = \omega_C^2 \cdot M_C \tag{3}$$

To capture all different cases from $FR = 0$ (empty vessel) to $FR = 1$ (full vessel), the [0, 1] range was discretized into seven intervals: a long one to capture the lower values, namely [0, 0.4), and six of length 0.1 for the higher ones, where the structure remains vulnerable to seismic motion, namely [0.4, 0.5), ..., [0.90, 1.00]. A single value was selected to represent each interval, resulting to a set of fill ratio values as $FR = [0.35, 0.45, 0.55, 0.65, 0.75, 0.85, 0.95]$, as shown in Table 1. This set comprises the center of each of the shorter intervals, plus 0.35 for the lower (and longer) one. The reason behind the latter choice is that such low FR values are not likely to appear, and when they do, the resulting mostly empty vessel has minimal to negligible seismic vulnerability. Improving our modeling resolution by allocating more FR values in [0, 0.4) would only create more models that are practically invulnerable to the seismic hazard of the site, making no difference in the ensemble risk. Finally, for this welded steel structure, a damping of 2% was assumed at the impulsive mode.

3 Methodology outline

3.1 Fragility analysis

A high-fidelity seismic performance assessment invariably involves multiple nonlinear response-history analyses under one or more suites of ground motion records (e.g., [37, 38]). Their results are typically represented by sets of intensity measure (IM) versus EDP values, as generated by each analysis. An IM is a (typically scalar) variable that characterizes the intensity of the ground motion, such as the peak ground acceleration or the 5% damped spectral acceleration at a period of interest. On the other hand, one or more EDPs, such as drifts, strains, or moments and forces are employed to capture the structural response of interest given the IM. Due to the logistic complexity of handling multiple such IM-EDP sets, one typically employs fragility functions to summarize them into a single usable curve that characterizes each LS of interest. The process of calculating so-called analytical (by virtue of using analysis rather than empirical data) fragility curves via response-history analyses is well established in current literature (e.g., [39–45]). The fragility curve is essentially a function of the IM that relates the probability of violating the LS of interest given that an event of the given IM has occurred. In functional form, it can be expressed as:

$$F_{LS}(IM) = P[LS \text{ violated } | IM] = P[D > C_{LS} | IM] \tag{4}$$

where

$F(\cdot)$ is the cumulative distribution function of its argument,
D is the demand expressed in EDP terms, and
C_{LS} is the capacity threshold expressed in EDP terms paired to a specific LS.
For the typical lognormality assumption [46], fragilities may be expressed as:

$$P[D > C_{LS} | IM] = \Phi\left(\frac{\ln IM - \ln IM_{LS50}}{\beta_{LS}}\right) \tag{5}$$

where

IM_{LS50} is the median (50%) intensity measure required to exceed LS and
β_{LS} is the lognormal dispersion, or the standard deviation of the natural logarithm of the set of IM values (one per ground motion employed) that cause LS violation.

3.2 Intensity measures and record selection

Four different scalar IMs are adopted in our study, as pressure vessel assessment is often only a part of a full-scale refinery assessment study. Thus, offering multiple IM options can help exploit the results within different analysis settings. The IMs employed are:

(a) The geomean average spectral acceleration, $AvgS_a$, defined as the geometric mean of multiple spectral acceleration values of both horizontal ground motion components taken across a range of equally spaced periods spanning between 0.1 s and 1.0 s, with an increment of 0.1 s.
(b) The geomean spectral acceleration at the (fictional) period of T_{tot}, essentially disregarding the sloshing effects, $S_a(T_{tot})$.
(c) The geomean spectral acceleration at the impulsive period T_I, $S_a(T_I)$.
(d) The geomean peak ground acceleration (PGA).

All four IMs employ the geomean of both horizontal components, while all spectral accelerations are estimated for 5% viscous damping, to comply with available ground motion prediction models. In general, the spectral acceleration IMs can be considered as asset-aware measures, since they involve vessel characteristics, while PGA is asset-agnostic. $AvgS_a$ is an in-between case, since it involves a range of periods rather than a singular value attributed to the structure. Still, it can be considered as a moderately asset-aware case, since the range is selected to encompass the periods of a single asset or envelop the periods of many assets of interest.

To properly calculate the EDP values via IDA, a set of 30 "ordinary" (i.e., non-pulse like, non-long duration) natural ground motion records is selected via the conditional spectrum approach [47, 48], considering the horizontal components of the excitation in both orthogonal directions. The specific record sequence numbers (RSN) from the NGA-West2 database [49] appear in Karaferis et al. [50]. This record selection ensures that the ground motions will be hazard-consistent with the area where the pressure vessels are located, and it is further documented in Bakalis et al. [51], where the interested reader can find more details.

4 Demand and capacity assessment

To properly evaluate the performance of any structure, it is essential to define DSs that are representative of the structure's main modes of damage or failure. Additionally, the EDPs calculated from the analyses performed must be able to convey the information needed for damage quantification and to allow the evaluation of the structure's condition in engineering terms. LSs should also be defined as capacity thresholds between the different damage states.

At first, a first-mode load pattern is adopted to perform static pushover analysis. This allows for a uniform evaluation of the structure's behavior, given a single EDP, namely the horizontal displacement, d_v, calculated at the center of the spherical vessel at the location of the impulsive mass. This is a reasonable simplification since d_v essentially determines (maps one-to-one to) all other EDPs; in other words, the pressure vessel model fully conforms to the theoretical framework underlying the nonlinear static procedure. Therefore, d_v can be employed as a proxy for any other EDP. Note that for the static pushover the direction of the horizontal load pattern (e.g., X) also defines the direction d_v (also X) for this fully symmetric structure. Still, one needs to generalize this to allow connecting with the 3D loading of response-history analysis. Thus, d_v is generally calculated as the square-root-sum-of-squares (SRSS) combination of the X and Y responses.

The resulting pushover capacity curve is presented in Fig. 3a representing all the different FRs, while the corresponding stiffness–displacement curves appear in Fig. 3b. As expected, the structure's stiffness does not change for different FRs, since the latter only concern the mass. Therefore, we can now look for distinctive changes in the global stiffness of the structure, which generally correspond to different consequences and the need for different post-event intervention actions, to define a single set of DSs for all FR cases. Specifically, three progressive and distinct DSs are identified as shown in Fig. 3.

DS1 occurs when any of the structure's braces reaches its yield strength for the first time. At this point the structural stability of the structure is retained, though after the event the brace(s) that yielded will probably need to be replaced. Therefore, minor interventions will be required. The vessel progresses to DS2 when the majority (i.e., more than 50%) of the braces in tension have reached or exceeded their yielding point. This suggests non-negligible damages to the structure, requiring replacement of most braces as well as repairing some local deformations in the columns. The vessel itself is not expected to lose its structural integrity given that the column-to-shell connection is assumed to hold. Still, this kind of damage would require major repairs to restore the vessel's operability. It should be noted that in DS2 minor leakage cannot be ruled out, but given the limitations in the modeling of the vessel this cannot be addressed without resorting to empirical data from similar vessels in past events. Finally, DS3 occurs when any of the braces fails in tension. In this case, the structure suffers a major loss of stiffness and strength, while plastification at the top part of the columns (at or above the uppermost bracing level) is expected almost immediately afterward. The vessel is essentially considered collapsed with major loss of containment expected. It should be noted that the columns do not fail before the braces since the former are generally overdesigned. Table 2 summarizes the above described DS classification along with the corresponding d_v threshold values.

To assess the demand, the 16/50/84% fractile IDA curves for the pressure vessel with $FR = 0.95$ are indicatively presented in Fig. 4, where d_v is plotted against the four different IMs considered. For any given level of the IM, these curves offer the value of d_v that has been exceeded by 16/50/84% of the ground motion records. The nonlinear behavior of the model can be easily observed for high levels of intensity, leading to changes in the fractile curve slopes and a rapid increase of dispersion.

5 Initial fragility results

5.1 Partial fragility curves

Fragility curves were calculated for each DS and each FR, termed "partial" as they pertain to a specific fill ratio that varies over time and thus can only partially characterize the entire structure. To account for any capacity-related uncertainties, 100 normally distributed capacity realizations were generated for each ground

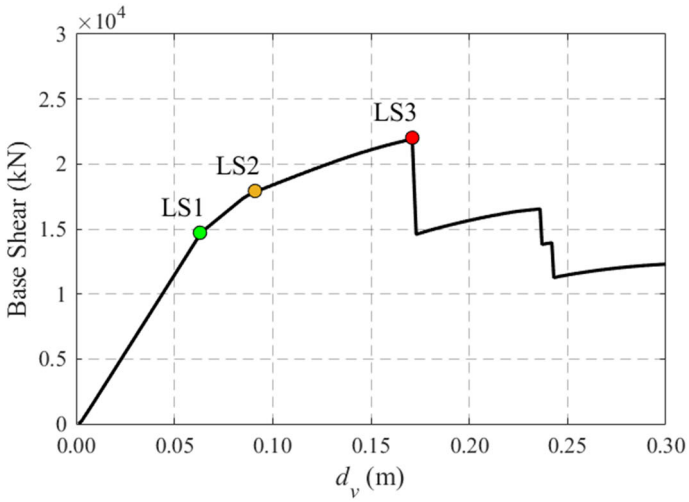

(a) Pushover capacity curve

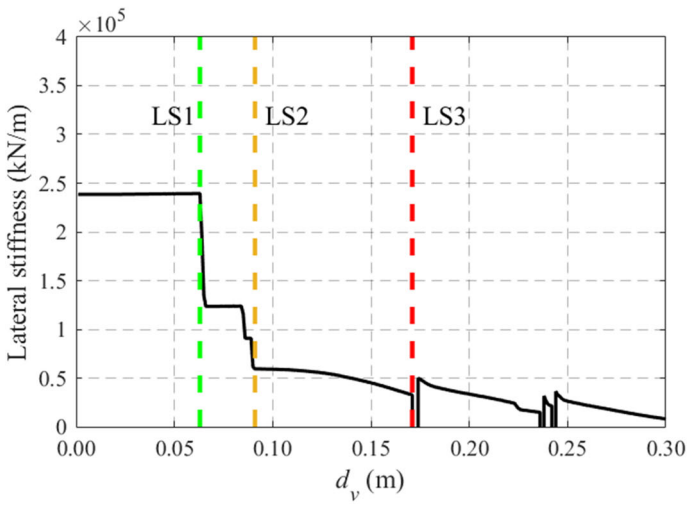

(b) Stiffness versus displacement curve

Fig. 3 Coincident **a** pushover curves and **b** stiffness–displacement curves for the spherical pressure vessel, regardless of filling ratio. Dot points and dashed vertical lines show the definition of the three LSs at the corresponding points of abrupt loss of stiffness

Table 2 DS classification and capacity thresholds in terms of displacement at the center of the spherical vessel

Damage state	Description	Displacement capacity
DS1	First yielding of any brace in tension	6.30 cm
DS2	Yielding of more than 50% of braces in tension	9.10 cm
DS3	Fracture of any brace	17.10 cm

motion record, assuming a 20% coefficient of variation around the median DS threshold values of Table 2. In Figs. 5, 6, and 7, the empirical cumulative distribution function data points along with the associated lognormally fitted [42] partial fragilities are presented, indicatively, for $FR = 0.95$, 0.75 and 0.55. In Table 3, the corresponding lognormal median and dispersion parameters are presented for all vessels examined (identical vessels with different *FR*s).

It is evident that for lower *FR*s the probability of exceedance (PoE) of any DS is lower given the same IM level, compared to vessels with higher *FR*s. Therefore, the damage a vessel sustains for any given IM is expected to be lower as well, if for example it is half empty compared to a full one. These substantial differences

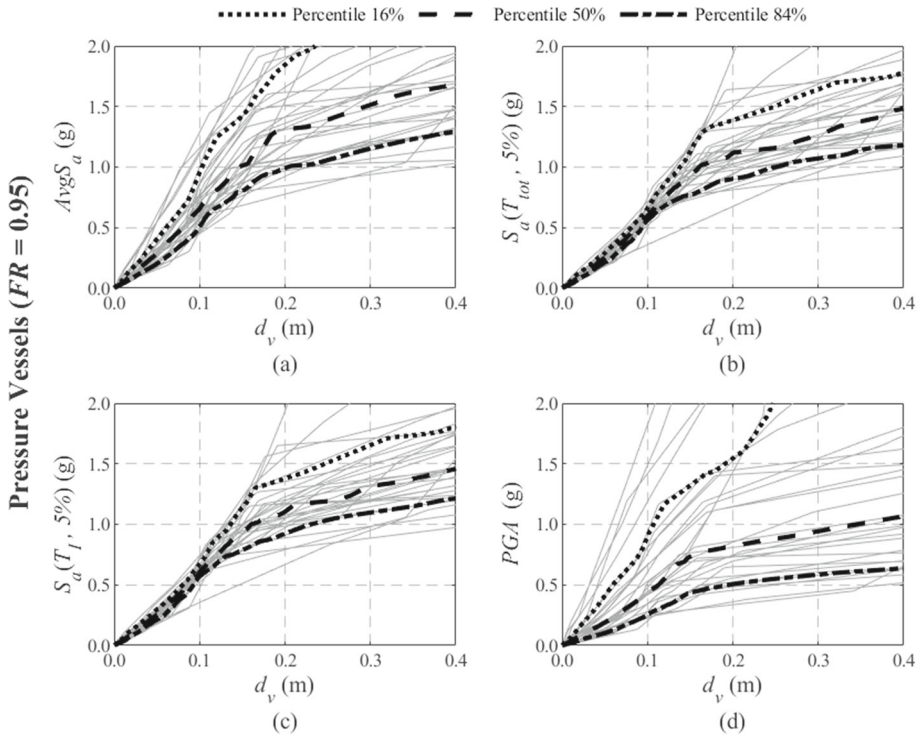

Fig. 4 The 16/50/84% fractile IDA curves of the pressure vessel for $FR = 0.95$ showing displacement d_v of the center of the spherical vessel against the IMs of **a** $AvgS_a$, **b** $Sa(T_{tot})$, **c** $Sa(T_1)$, and **d** PGA

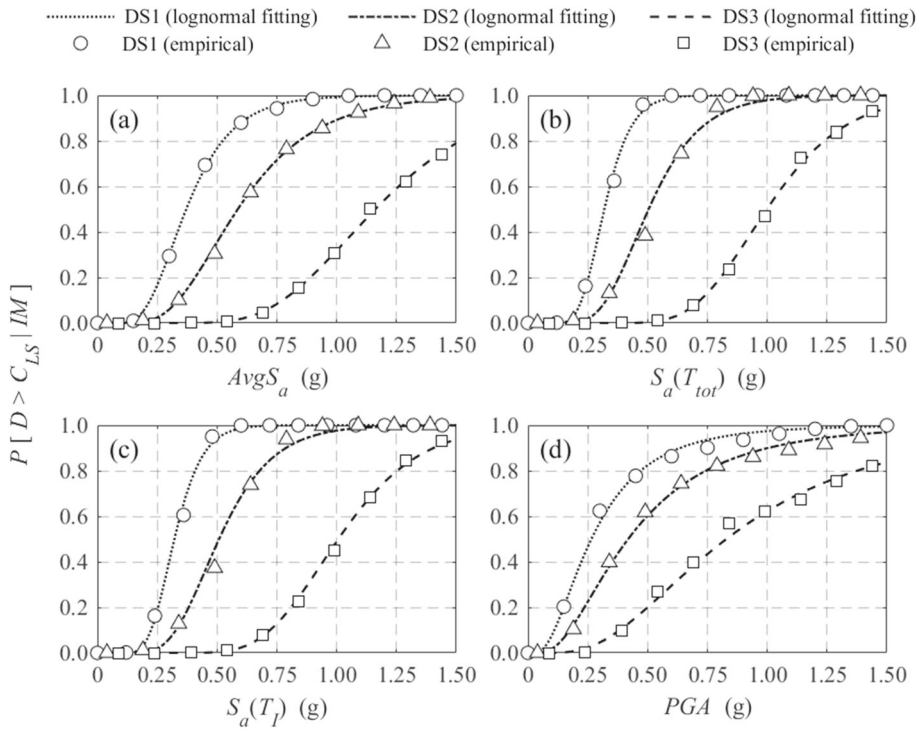

Fig. 5 Pressure vessel partial fragility curves for $FR = 0.95$ considering the selected four IMs

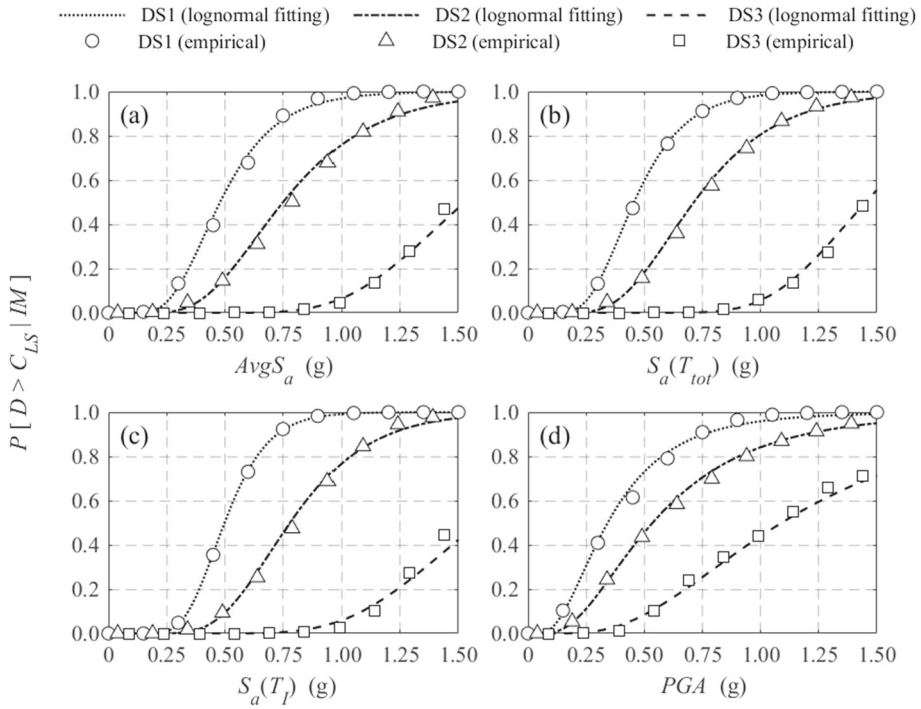

Fig. 6 Pressure vessel partial fragility curves for $FR = 0.75$ considering the selected four IMs

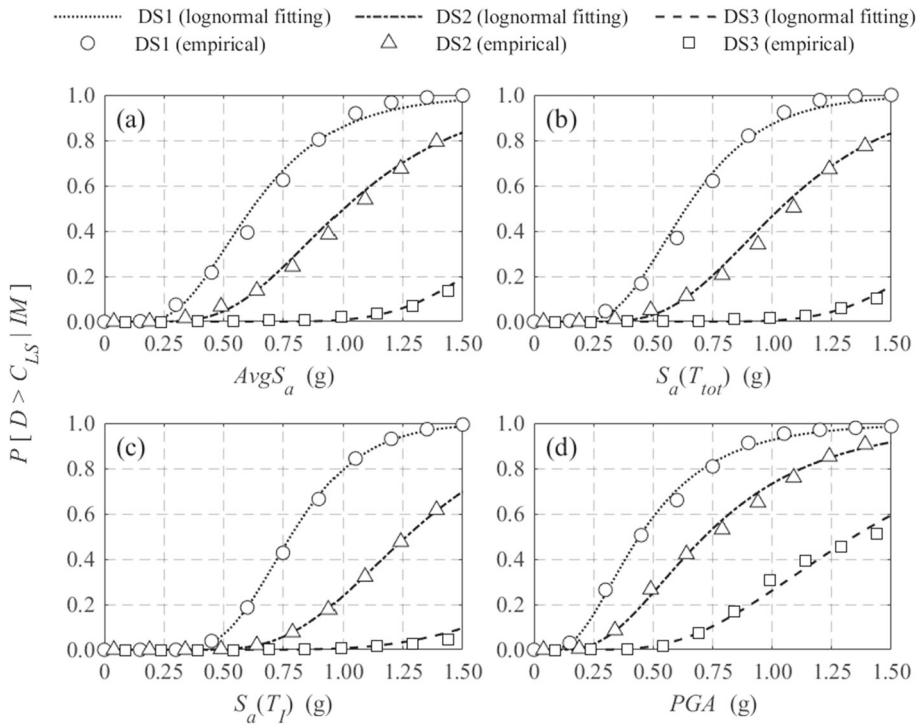

Fig. 7 Pressure vessel partial fragility curves for $FR = 0.55$ considering the selected four IMs

Table 3 Median ($\mu = IM_{LS50}$) and dispersion ($\sigma = \beta_{LS}$) of the lognormally fitted partial fragility curves for each *FR* and IM considered.

Damage states		$AvgS_a$		$S_a(T_{tot})$		$S_a(T_I)$		PGA	
		μ(g)	σ	μ(g)	σ	μ(g)	σ	μ(g)	σ
$FR = 0.95$	DS1	0.37	0.41	0.32	**0.28**	0.32	**0.28**	0.27	0.68
	DS2	0.59	0.43	0.50	**0.34**	0.51	**0.34**	0.42	0.68
	DS3	1.16	0.32	1.00	**0.26**	1.01	**0.26**	0.83	0.60
$FR = 0.85$	DS1	0.40	0.37	0.36	**0.28**	0.39	0.29	0.29	0.64
	DS2	0.66	0.42	0.60	**0.35**	0.64	0.36	0.47	0.66
	DS3	1.36	0.32	1.22	**0.23**	1.31	0.28	0.97	0.60
$FR = 0.75$	DS1	0.48	0.39	0.46	0.38	0.50	**0.29**	0.34	0.62
	DS2	0.75	0.41	0.71	0.39	0.78	**0.34**	0.54	0.62
	DS3	1.53	**0.28**	1.45	0.24	1.59	0.30	1.09	0.57
$FR = 0.65$	DS1	0.54	0.38	0.54	0.39	0.63	**0.31**	0.39	0.51
	DS2	0.84	0.37	0.83	0.39	0.97	**0.32**	0.60	0.52
	DS3	1.67	**0.27**	1.65	0.29	1.92	0.32	1.19	0.52
$FR = 0.55$	DS1	0.62	0.44	0.64	0.40	0.78	**0.30**	0.44	0.57
	DS2	1.00	0.41	1.03	0.39	1.26	**0.33**	0.72	0.54
	DS3	1.88	**0.26**	1.94	0.26	2.37	0.35	1.34	0.46
$FR = 0.45$	DS1	0.77	0.44	0.86	0.42	1.02	**0.30**	0.55	0.44
	DS2	1.18	0.44	1.32	0.41	1.56	**0.32**	0.85	0.44
	DS3	2.28	0.32	2.54	**0.29**	3.00	0.30	1.63	0.40
$FR = 0.35$	DS1	0.89	0.49	1.05	0.47	1.28	**0.33**	0.64	0.42
	DS2	1.31	0.48	1.54	0.46	1.87	**0.33**	0.93	0.42
	DS3	2.86	0.33	3.09	**0.27**	4.03	0.32	2.01	0.40

Dispersions in bold indicate the minimum values achieved per *FR* and DS

in PoE values should not be overlooked in an assessment study and consequently have to be properly accounted for. In other words, properly accounting for the variability introduced by an uncertain FR cannot be replaced by an ultra-conservative assumption that all vessels are fully filled in perpetuity.

5.2 IM selection discussion

The results have been presented so far using the selected four different IMs: (a) $AvgS_a$, (b) $S_a(T_{tot})$, (c) $S_a(T_I)$, and (d) PGA, all of which have their advantages and disadvantages. The most important piece of information is the interplay between the dominant structural period per each DS and the period (or period range) of the IMs, and how this affects the partial fragility dispersions in Table 3. In general, a lower dispersion is desirable, as it allows using fewer response-history analyses to achieve the same fidelity in the results, a property known as efficiency [52], while at the same time lowering the potential bias in the estimates [53], thus improving sufficiency.

Then, it should be little wonder that $S_a(T_I)$ is almost consistently the better choice for every single vessel for DS1 and DS2. For these states, there is little "period elongation" due to damage; thus, the impulsive period remains a good predictor of deformation, resulting in low dispersions. A close contender is $S_a(T_{tot})$, almost matching, or even momentarily exceeding, the performance of $S_a(T_I)$ for almost full vessels, as T_{tot} is about the same as T_I (see Table 1). Since T_{tot} is calculated assuming the liquid mass to be solid, the resulting period differs substantially from the impulsive one at low FR values, where a large percentage of the liquid participates in sloshing. Thus, $S_a(T_{tot})$ becomes suboptimal for lower FR where sloshing is important. Paradoxically, this increased T_{tot} can better match an "elongated" period at DS3, leading to the lowest dispersions for DS3 at $FR = 0.35, 0.45$ over all four IMs.

In terms of $AvgS_a$ the dispersion is more or less stable for any given DS across different FR, albeit somewhat higher compared to single period spectral ordinates: on average its dispersion is 1.2 times higher than $S_a(T_I)$ and 1.1 times higher than $S_a(T_{tot})$. By virtue of averaging spectral accelerations over a range of periods (0.1–1.0 s), $AvgS_a$ lacks the ability of $S_a(T_I)$ to match the impulsive period, which hurts its performance for low DSs. At the same time, it offers more stability in the more uncertain post-yield range, where for DS3 and $FR = 0.55{-}0.75$, $AvgS_a$ becomes optimal. Selecting a different range of periods that would better bracket the values of T_I encountered (and their elongated versions) could help to improve its performance, but it would remove its main advantage of being applicable to other structures that may be encountered in an oil refinery

as an integrated setting. Finally, PGA corresponds to an effective period of zero, progressively getting better as lower FRs are considered only because the eigenperiods of those vessels are lower and therefore closer to rigidity. Still, PGA consistently produces much higher dispersions compared to the other IM cases: on average 1.7 times higher than $S_a(T_I)$ and 1.4 times higher than $AvgS_a$.

Overall, as a rough metric to characterize each IM type, we can use the average of dispersions across all DSs and FR values resulting to 0.38 for $AvgS_a$, 0.34 for $S_a(T_{tot})$, 0.31 for $S_a(T_I)$ and 0.54 for PGA. Even though it is a particularly rough comparison, it seems that the best predictor should be $S_a(T_I)$ for any singular vessel. Yet, choosing a structure-specific and even FR-specific IM, constrains the applicability and generality of the assessment in case a portfolio of assets is considered. Even if we assume that one somehow possesses knowledge of the actual FR at the time of an event (or at least most events), taking advantage of this to select the optimal $S_a(T_I)$ per asset would remain highly impractical: the analyst would need to produce hazard results parameterized to different "optimal" IMs to best capture tanks of different FRs as well as all other refinery structures, potentially also requiring spatial correlation and cross-correlation considerations. For these cases, adopting a single moderately structure-specific IM can offer substantial logistical and computational benefits, and it seems that $AvgSa$ would generally be the better choice, provided that a suitable range of periods is selected for all structures considered. Even in this study, where a fairly broad range was assumed to retain applicability for other refinery assets, the dispersions calculated are acceptable. PGA could also offer this wide applicability, but at the cost of higher dispersions for all FR values that matter.

5.3 Sloshing effect contribution

Another critical remark to be made is the importance of introducing to the model the sloshing effects. The mass of the vessel and how it is divided between the impulsive and sloshing parts given each *FR* examined, can heavily affect the response. In Fig. 8, the results for the first three *FR*s are illustrated, with and without considering the sloshing, in the latter case considering the full mass of the liquid as impulsive. Only *PGA* and $AvgS_a$ are shown, excluding $S_a(T_I)$ and $S_a(T_{tot})$ to avoid any issues of actual versus apparent periods for the non-sloshing model.

As observed, the sloshing behavior only mildly affects a vessel that is nearly full, but as the *FR* lowers, the partial fragilities become much more conservative compared to what would be the more realistic ones, derived for the sloshing model. One can argue that disregarding the sloshing behavior in design would not be a problem, given that the vessels are assumed to be full for seismic verifications. Still, for risk assessment purposes, excluding these lower FR values would lead to overconservative results and, therefore, to an unrealistically increased risk.

6 System fragilities

Introducing multiple partial fragilities for a single pressure vessel is an accurate but also impractical representation for large-scale risk analysis. To overcome this obstacle, there are two levels of integration that one can employ to assist practical application, going from the partial to the system fragility. First, one needs to integrate the *FR*-dependent partial fragilities into a single combined fragility that characterizes the single structure. Second, given a group of multiple similar, or even identical, pressure vessels (see Fig. 1) one can undertake an additional integration to offer a single group-of-vessels ensemble fragility to represent them together.

6.1 Single-vessel combined fragility

Depending on the scope of the assessment, three cases can be identified on how to account for *FR*-dependence when determining a single fragility of a pressure vessel. The most simplistic one would be to employ the worst fragility, assuming that the vessel would be near full during an earthquake (e.g., $FR = 0.95$). Alternatively, one could pick a representative medium or most frequent FR value (e.g., $FR = 0.65$) using engineering judgment or experience. Such approaches, though, simplify the problem by essentially looking at only one of its aspects and discarding the rest. In turn, the results could become too conservative, too optimistic, or simply lacking the proper level of variance, thus invalidating the entire process of striving to achieve high fidelity.

A better idea is to combine the different partial fragilities into a single fragility curve per DS, explicitly incorporating the relative likelihood of different *FR* values. When combining lognormally fitted fragilities,

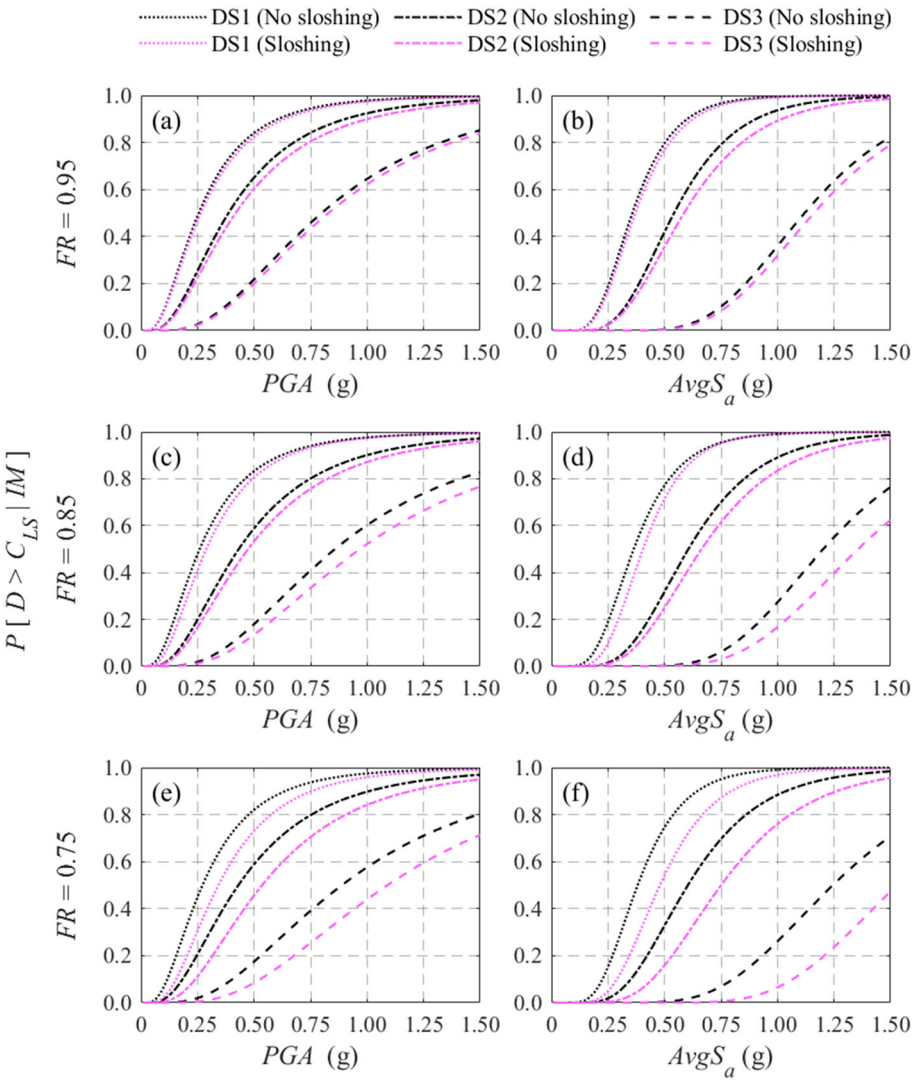

Fig. 8 Comparison of partial fragilities with and without considering the sloshing effect for three levels of FR and the IMs of **a**, **c**, **e** PGA and **b**, **d**, **f** $AvgS_a$

the laws of total expectation and variance [54, 55] can facilitate this integration by allowing us to calculate an overall median and dispersion that characterizes the new combined fragility. For the case at hand, weights of $w_i = [0.2, 0.2, 0.2, 0.1, 0.1, 0.1, 0.1]$ were assigned to the partial fragilities calculated for $FR = [0.95, 0.85, 0.75, 0.65, 0.55, 0.45, 0.35]$ accordingly, meaning that the three higher FRs are twice as likely to occur compared to the others. In practice, the proper determination of such weights requires engineering judgment and some data on the operation of the facility, which should be readily available in any practical situation. Then, the law of total expectation stipulates that the overall logarithmic mean is

$$\ln IM_{LS50} = \sum_{i=1}^{7} w_i \ln IM_{LS50,i} \tag{6}$$

while, per the law of total variance, the overall dispersion becomes

$$\beta_{LS} = \sqrt{\sum_{i=1}^{7} w_i \left(\beta_{LS,i}\right)^2 + \sum_{i=1}^{7} w_i \left(\ln IM_{LS50,i} - \ln IM_{LS50}\right)^2} \tag{7}$$

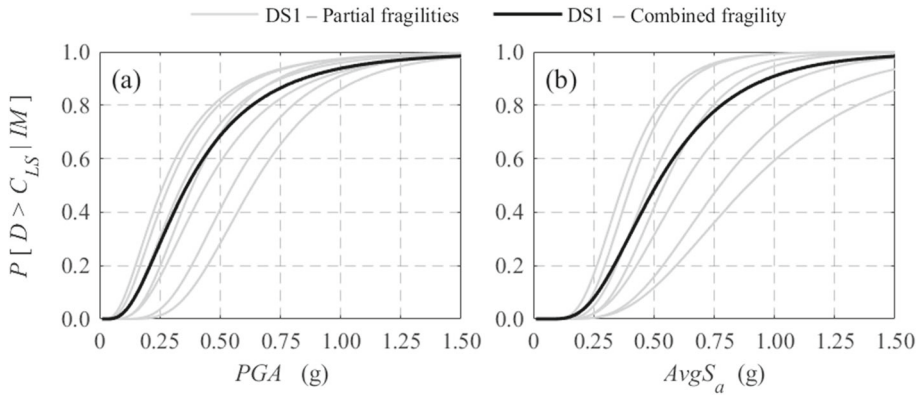

Fig. 9 Fragility combination example for DS1 and two IMs. The light gray fragilities estimated for each *FR* are combined per Eqs. (6) and (7) to deliver the combined fragility in black

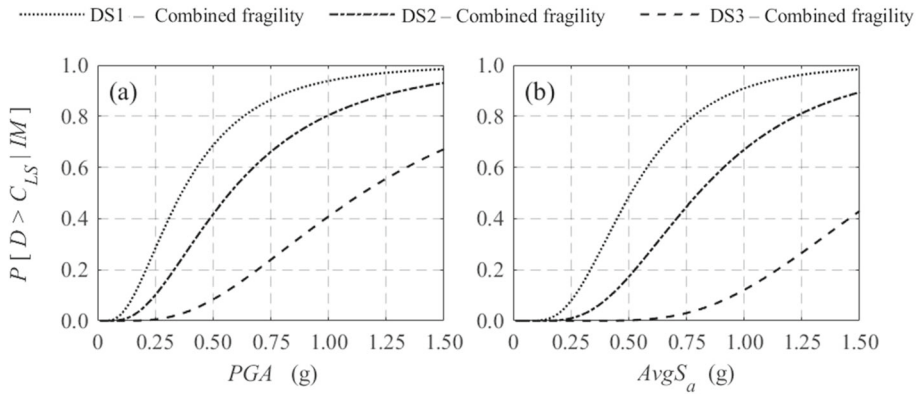

Fig. 10 The resulting combined fragilities of a single vessel for all DS and two IMs

Table 4 Median ($\mu = IM_{LS50}$) and dispersion ($\sigma = \beta_{LS}$) of the lognormal combined fragility curves for a single vessel

Damage states		PGA		$AvgS_a$	
		μ(g)	σ	μ(g)	σ
Single vessel	DS1	0.36	0.66	0.51	0.50
	DS2	0.57	0.65	0.80	0.50
	DS3	1.15	0.60	1.61	0.41

In order to combine the partials, one needs to express them in the same IM terms, wherein lies the advantage of $AvgSa$ and PGA. Of course, one could employ some averaged value of T_I or T_{tot}, but this would automatically negate most of the advantages enjoyed by the structure-specific $S_a(T_I)$ and $S_a(T_{tot})$. Hereinafter, all results will be shown only in terms of $AvgS_a$ and PGA.

The partial fragilities for DS1 and each *FR* are presented in Fig. 9 alongside the combined DS1 fragility of the vessel. As observed, the heavier weighting of the high FR values (leftmost partial fragilities) clearly draws the combined fragility to the left, i.e., to lower IM values. In Fig. 10 the combined fragilities are showcased for all DSs, while in Table 4 the lognormal parameters for those fragilities calculated are presented. For $AvgS_a$, where partials of similar dispersion are combined, the resulting combined fragilities have a higher dispersion than any of their constituents. For PGA, the same cannot be claimed, as partials of highly differing dispersions are combined. Still, the overall fragility retains a dispersion on the high end, and higher than most partials. That is, the combination of the partial fragilities manages to propagate the uncertainty in the value of FR to the single-vessel representation, generally increasing the variability one would receive from a single FR value.

6.2 Group-of-vessels ensemble fragility

Pressure vessels often come in groups of multiples within a refinery or storage facility (tank farm), potentially only differing in their filling ratios at any given time due to operational reasons. In general, there are two paths to assess such a group of vessels: (a) numerically simulating FR values for each vessel and using the partial fragility functions to define the overall risk or (b) analytically deriving an ensemble fragility function based on the single-vessel combined fragility. The former is by far the more cumbersome and higher-fidelity approach. Unfortunately, it is also the one that cannot be applied in practical situations, as most analysts (e.g., [11, 13]) provide single-vessel fragilities, rather than the partial ones introduced herein. On the other hand, the analytical approach employs such single-vessel fragilities, regardless of whether they were derived on the basis of partials or otherwise, and it is considerably simpler to use. Yet, at the same time its mode of implementation depends on the correlation of the filling ratios in the individual vessels. Simply put, whether all vessels tend to be uniformly filled at all times or not makes a difference on how one analytically derives the ensemble fragility.

As a case study, let us consider the four pressure vessels of Fig. 1. They are located close enough (typically for safety reasons of the entire facility) that during a seismic event they are to be affected by the same level of intensity (spatial variability of the ground motion is insignificant). Following the numerical simulation approach, Monte Carlo is employed to generate 200 realizations of the four pressure vessels, assigning an FR value to each.

At first, full correlation is assumed, meaning that all four vessels have the same (random) FR for any given realization of the group of four. Thus, for a specific IM level, e.g., for $PGA = 0.3$g, all vessels will have the same PoE for a specific DS and realization, depending on the FR that has been randomly assigned to them. In addition, their uncertain capacity thresholds are similarly assumed to be fully correlated due to employing the same design, contractor, construction quality, and level of maintenance. In other words, for any seismic event, the four tanks always reach the same DS. So, the PoE of the ensemble per realization is the same as the PoE calculated for any of the four vessels. Unsurprisingly, assuming full correlation means that the ensemble PoE is identical to the PoE of the individual.

The results for DS1 and $PGA = 0.3$g are presented in Fig. 11 for each of 200 realizations. Since these are equiprobable, the numerically estimated (ensemble) PoE for all four vessels is simply their average. In terms of the analytical derivation, one need only use the PoE of the single-vessel combined fragility. Clearly, the analytical approximation is quite accurate, with any minor difference being only an artifact of the limited sample of realizations employed.

Figure 12 shows the resulting numerical and analytical ensemble-fragilities employing the aforementioned procedures for all IM levels in terms of PGA and $AvgS_a$. The two approaches are a close match, as expected. It should be noted though that there is high variability between the individual realization results (e.g., Fig. 11), which largely disappears due to the summarization implied in the fragility. When one evaluates the operation of the entire facility, there can be significant value to considering the individual realizations on a one-by-one basis, given the detrimental effects of any large-scale failure of a single asset. Still, this is a known side-effect of using fragilities and will not be explored further.

Now, let us consider zero correlation between the different vessels, both in terms of FRs and in terms of DS capacity thresholds. This would in general be a more realistic case, where there are differences in the filling level and structural state of each tank. The latter can be attributed primarily, among other, to material variabilities, construction quality issues, or due to the tanks undergoing regular maintenance in a sequential order, which is the typical case for operational reasons. This means that each specific vessel now has a different probability of exceedance provided by the partial fragility that corresponds to the random FR assigned to it in each realization. As a consequence, after any seismic event the four vessels may have different DSs.

In order to be able to define a global ensemble fragility, one should first define a global DS to characterize the ensemble. Herein, the four vessels are treated as a series system, meaning that failure in any of the four structures is treated as failure of the ensemble. Concisely, the worst DS of any tank becomes the DS of the group. This is an accurate assumption for any DS involving leakage, mainly DS3, as loss of containment typically leads to catastrophic consequences for the entire group. It is less so for DS1, or even DS2, where mostly repairable damages are expected, rather than catastrophic cascading effects.

To properly account for the uncorrelated capacity thresholds, the numerical approach requires a second layer of Monte Carlo, whereby for each of the original 200 FR realizations, further 1000 realizations of DS-exceedance are generated, based on the partial fragility PoE. For example, let us say that for a single vessel with given FR and IM level, the partial fragility for DS1 yields PoE $= 70\%$. Then, 70% of the realizations for this vessel are designated as having exceeded DS1. Note that this discounts the effect of waveform correlation,

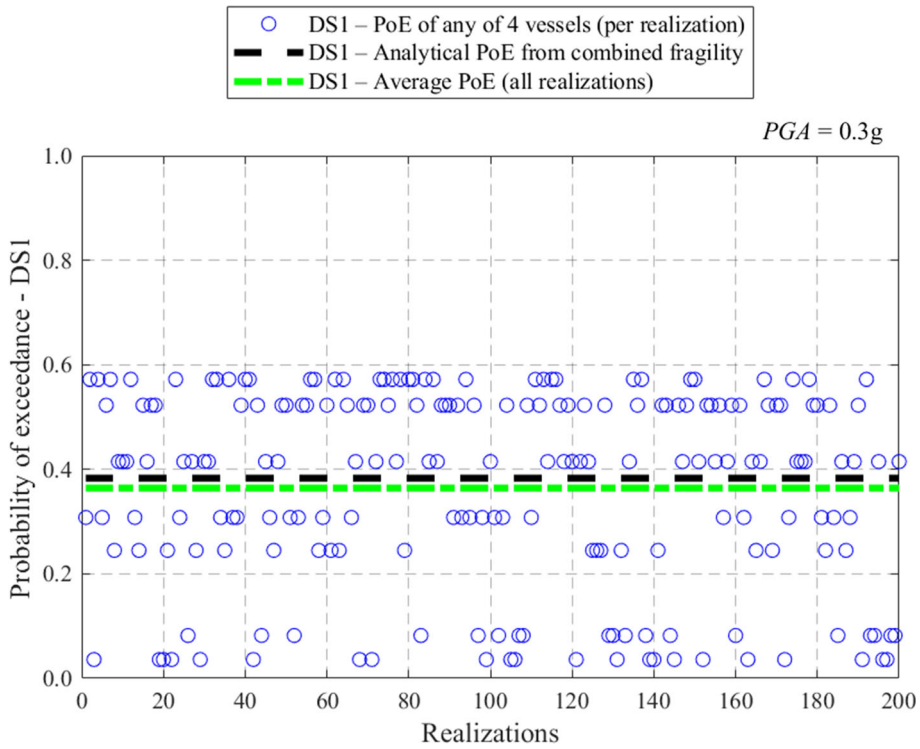

Fig. 11 Comparison of the numerical versus the analytical approach for the ensemble probability of exceeding DS1, given full FR correlation and $PGA = 0.3$g. The average of 200 realizations matches the analytical result

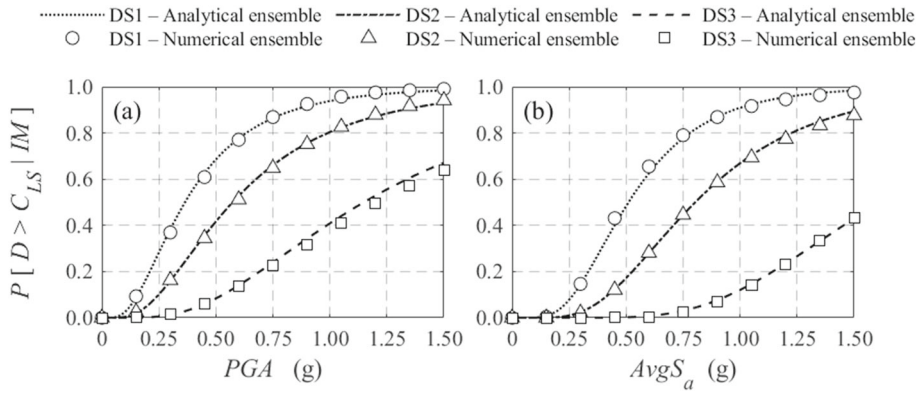

Fig. 12 Four-tank ensemble fragilities assuming full correlation: Comparison between the analytically estimated (via Eqs. 6–7) combined fragility for a single tank and the numerically estimated one (via Monte Carlo) for the ensemble of four. Perfect correlation means that assessing one tank versus an ensemble is the same, at least in terms of PoE

as one would reasonably expect all four vessels to be subjected to the same ground motion, rather than just the same IM level, treating ground motion variability and DS capacity variability in the same way. Investigating the consequences of this is beyond the scope of our research, but it should certainly be expected to (conservatively) increase the variability in the system. By combining these 4×1000 sub-realizations, a single ensemble PoE value is estimated for each one of the 200 realizations of the group, assuming that any failure in one vessel also means failure of the group of four. Given that again the realizations are considered equiprobable, the average value of the ensemble PoE results characterizes the group of four for any given IM level. Figure 13 shows the results for the exceedance of DS1 for $PGA = 0.3$g. Notably, the ensemble PoE is higher than the PoE of any individual vessel per realization. While one would reasonably expect the tank with the highest FR to dominate the ensemble PoE, the lack of correlation in a series system means that there is always a chance for some vessels with lower FR to get more damage in any given event, e.g., by virtue of construction defects or delayed maintenance.

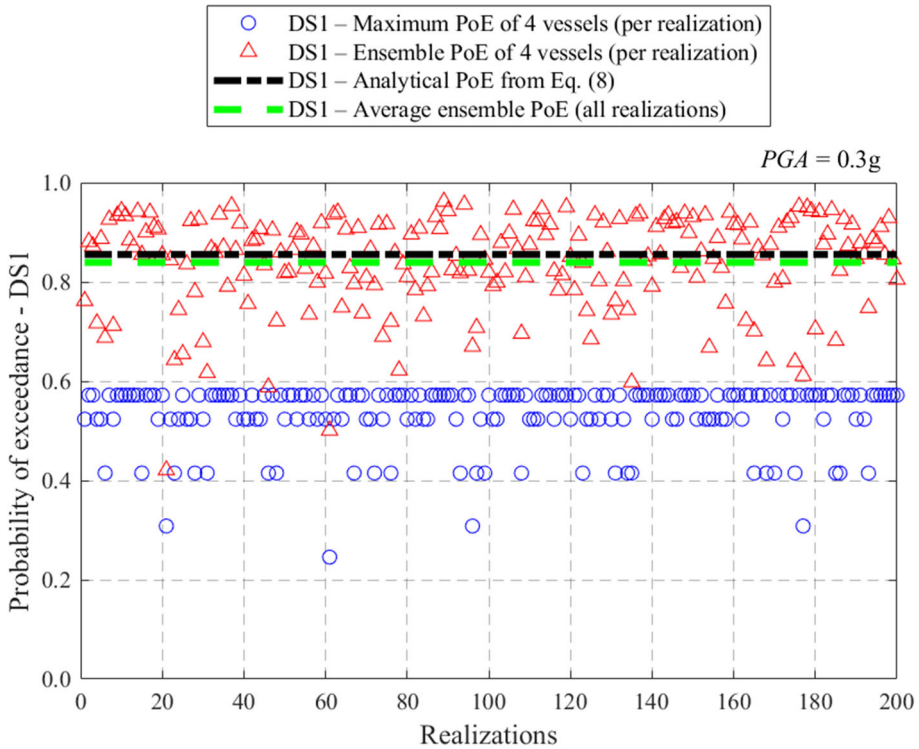

Fig. 13 Comparison of the numerical versus the analytical approach for the ensemble probability of exceeding DS1, given zero FR correlation and $PGA = 0.3$g. The average of 200 realizations matches the analytical result, both exceeding the PoEs of any individual vessel

Table 5 Median ($\mu = IM_{LS50}$) and dispersion ($\sigma = \beta_{LS}$) of ensemble fragility curves for the group of four pressure vessels

Damage states		PGA		$AvgS_a$	
		μ(g)	σ	μ(g)	σ
4-vessel system	DS1	0.19	0.45	0.31	0.35
	DS2	0.30	0.45	0.49	0.35
	DS3	0.63	0.42	1.07	0.28

For the analytical approximation, one needs to employ a logical OR combination (or union) of four identical single-vessel combined fragilities. This is typical for series systems, and it is easily resolved by taking the inverse route, meaning that failure of any of the four vessels is the negative of having all four vessels without failure [55]:

$$P(\text{at least one vessel fails}) = 1 - P(\text{no vessel fails}) = 1 - \prod_{i=1}^{N} P(\text{vessel } i \text{ does not fail}) = 1 - (1-p)^N \tag{8}$$

where N is number of vessels with the same (single-vessel combined) fragility and p the PoE of each individual vessel. As Fig. 13 attests, the results closely match the numerical approach.

Note that Eq. (8) only offers point-by-point estimates, rather than the full fragility definition provided by Eqs. (6) and (7) for full correlation. Thus, a lognormal fit is applied to the analytical assessment results of this case to calculate the parameters of the ensemble fragilities for the three DSs (see Table 5). In Fig. 14, the resulting fragilities are presented for both the analytical and the numerical approach showing an excellent match. In comparing the full (Table 4) versus zero correlation (Table 5) cases, the latter is a clearly more vulnerable condition for the group. The fragility medians are decreased by 40–50% when adopting zero correlations, while dispersions are also lowered by about 30% in all cases. In other words, zero correlation makes the group fail earlier and with more certainty.

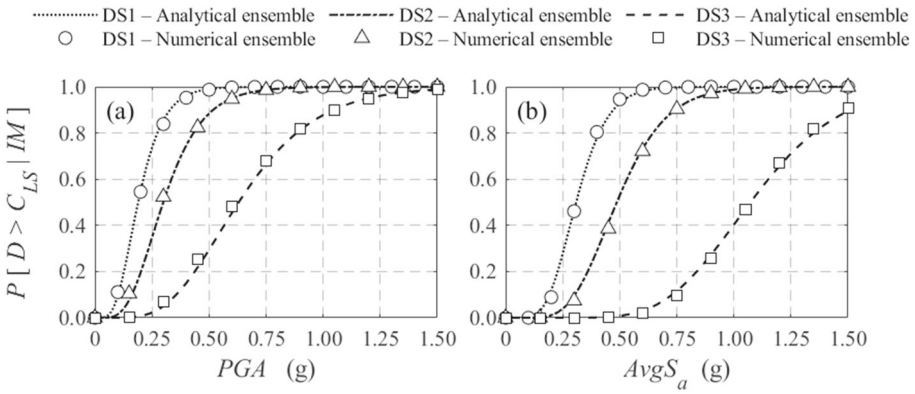

Fig. 14 Four-tank ensemble fragilities assuming zero correlation: Comparison between the analytically estimated (via Eq. (8), $N = 4$) ensemble fragility of four tanks and the numerically estimated one (via Monte Carlo). Zero correlation increases the probability of failure, needing a series-system combination for accurate assessment

7 Conclusions

A comprehensive study was performed for identifying the effect of the fill ratio and its correlation within a group of spherical pressure vessels. The main findings and contributions of the study are the following:

- A reduced-order mechanical model can efficiently capture the effect of the fill ratio on the vessel performance. Although in design the most critical state of the vessel is when it is full, from an assessment perspective a realistic representation of the vessel's response during a seismic event should account for the fact that the vessel behaves very differently when it is full, half-full or almost empty. It should be stated that a reduced-order model can arguably capture some of the most critical seismically induced failure modes, aiming toward computational efficiency; still, it may not account for localized failure modes that a detailed finite element model could capture, such as weld or gusset plate failures and local buckling, unless particular care is taken to explicitly incorporate them, e.g., via phenomenological macro-elements.
- Intensity measure (IM) selection for fragility analysis is dependent on the assessment's aims and objectives. While the spectral acceleration at the impulsive period is (near) optimal for given fill ratios, a moderately asset-aware IM, such as an average spectral acceleration, is a more versatile approach when considering multiple fill ratios, as well as different assets within an entire facility.
- Using fill-ratio-dependent partial fragilities within a comprehensive Monte Carlo simulation is arguably the optimal option for incorporating correlation in ground motions, structural properties, and fill ratios. Still, analytical approaches to determine single-vessel combined fragilities, as well as ensemble fragilities for groups of tanks remain viable, even though they are only matching the Monte Carlo results on average. Moreover, in the latter case regarding groups of tanks, ensemble fragilities are only practical for the edge cases of full or zero correlation of a series system. In any case, one cannot provide accurate estimates with either option without having data on the quantities stored in the tanks, or at least understanding the operation of the tank group within the facility and exercising some engineering judgement to determine weights for the different fill ratios and associated partial fragilities.

Acknowledgments The authors would like to thank Ms. E. Vourlakou for preparing the images of the structures and the model.

Funding Open access funding provided by HEAL-Link Greece. Financial support has been provided by the European Commission through the Horizon Europe Program, Project "PLOTO—Deployment and Assessment of Predictive modelling, environmentally sustainable and emerging digital technologies and tools for improving the resilience of IWW against climate change and other extremes" (Grant Agreement No. 101069941) and by the Hellenic Foundation for Research and Innovation (H.F.R.I.) under the "2nd Call for H.F.R.I. Research Projects to support Faculty Members & Researchers", Project "TwinCity: Climate-Aware Risk and Resilience Assessment of Urban Areas under Multiple Environmental Stressors via MultiTiered Digital City Twinning" (Grant Agreement Number: 2515).

Data availability Some or all data, models, or codes that support the findings of this study are available from the corresponding author upon reasonable request.

Declarations

Conflict of interest The authors have no relevant financial or non-financial interests to disclose.

Open Access This article is licensed under a Creative Commons Attribution 4.0 International License, which permits use, sharing, adaptation, distribution and reproduction in any medium or format, as long as you give appropriate credit to the original author(s) and the source, provide a link to the Creative Commons licence, and indicate if changes were made. The images or other third party material in this article are included in the article's Creative Commons licence, unless indicated otherwise in a credit line to the material. If material is not included in the article's Creative Commons licence and your intended use is not permitted by statutory regulation or exceeds the permitted use, you will need to obtain permission directly from the copyright holder. To view a copy of this licence, visit http://creativecommons.org/licenses/by/4.0/.

References

1. Moss, D.R.: Pressure Vessel Design Manual: Illustrated Procedures for Solving Major Pressure Vessel Design Problems, 3rd edn. Gulf Professional Publishing Elsevier, London (2004). https://doi.org/10.1016/B978-0-7506-7740-0.X5000-8
2. Eurocode 8: Design of Structures for Earthquakes Resistance, Part 4: Silos, Tanks and Pipelines. EN1998–4. European Committee for Standardization (CEN), Brussels (2006). https://eurocodes.jrc.ec.europa.eu/EN-Eurocodes/eurocode-8-design-structures-earthquake-resistance?id=138
3. Wieschollek, M., Kopp, M., Hoffmeister, B., Feldmann, M.: Seismic design of spherical liquid storage tanks. In: III ECCOMAS Thematic Conference on Computational Methods in Structural Dynamics and Earthquake Engineering, (COMPDYN2011), Corfu, Greece (2011)
4. Wieschollek, M., Diamanti, K., Pinkawa, M., Hoffmeister, B., Feldmann, M.: Guidelines for seismic design and analysis of pressure vessels. In: Pressure Vessels and Piping Conference, Vol. 55744, p. V008T08A015. American Society of Mechanical Engineers (2013). https://doi.org/10.1115/PVP2013-97435
5. Wieschollek, M., Pinkawa, M., Hoffmeister, B., Feldmann, M.: Seismic design of spherical pressure vessels. In: Seismic Design of Industrial Facilities: Proceedings of the International Conference on Seismic Design of Industrial Facilities (SeDIF-Conference), pp. 417–428. Springer Fachmedien Wiesbaden (2014). https://doi.org/10.1007/978-3-658-02810-7_35
6. Li, X., Chen, Z., Wang, W., Jing, W., Shao, S.: Research on structure security of a spherical tank under wind and seismic effect. In Pressure Vessels and Piping Conference, Vol. 55003, pp. 489–496. American Society of Mechanical Engineers (2012). https://doi.org/10.1115/PVP2012-78210
7. Yang, Z., Zhang, D., Guo, L., Yang, B., Wang, G.: Seismic performance analysis of the large spherical tank. In: Pressure Vessels and Piping Conference, Vol. 46001, p. V003T03A047. American Society of Mechanical Engineers (2014). https://doi.org/10.1115/PVP2014-28653
8. Ohno, T., Kobayashi, N., Oyamada, K.: Seismic resistance capacity on pipe braced supporting frame of spherical tank. In: Pressure Vessels and Piping Conference, Vol. 57034, p. V008T08A028. American Society of Mechanical Engineers (2015). https://doi.org/10.1115/PVP2015-45207
9. Fiore, A., Demartino, C., Greco, R., Rago, C., Sulpizio, C., Vanzi, I.: Seismic performance of spherical liquid storage tanks: a case study. Int. J. Adv. Struct. Eng. **10**, 121–130 (2018). https://doi.org/10.1007/s40091-018-0185-1
10. Ma, Z., Xiao, G., Zhang, M., Zhang, H., Du, R.: Comparative study on seismic response analysis methods of spherical tanks. In: Pressure Vessels and Piping Conference, Vol. 83839, p. V003T03A071. American Society of Mechanical Engineers (2020). https://doi.org/10.1115/PVP2020-21129
11. Moschonas, I., Karakostas, C., Lekidis, V., Papadopoulos, S.: Investigation of seismic vulnerability of industrial pressure vessels. In: Second European Conference on Earthquake Engineering and Seismology (2ECEES), pp. 25–29. Istanbul August. (2014)
12. Karakostas, C. Z., Moschonas, I. F., Lekidis, V. A., Papadopoulos, S. P. Seismic performance of industrial pressure vessels: Parametric investigation of simplified modeling approaches for vulnerability assessment. In: Proceedings of 5th International Conference on Computational Methods in Structural Dynamics and Earthquake Engineering (COMPDYN 2015), pp. 2021–2037. Crete Island, Greece (2015)
13. Öztürk, S., Akgül, K., Sarı, A.: Seismic fragility and behavior of spherical pressure vessels. In: Pressure Vessels and Piping Conference, Vol. 85352, p. V005T08A019. American Society of Mechanical Engineers (2021). https://doi.org/10.1115/PVP2021-61069
14. Yazdanian, M., Ingham, J.M., Kahanek, C., Dizhur, D.: Damage to flat-based wine storage tanks in the 2013 and 2016 New Zealand earthquakes. J. Constr. Steel Res. **168**, 105983 (2020a). https://doi.org/10.1016/j.jcsr.2020.105983
15. Yazdanian, M., Ingham, J.M., Kahanek, C., Dizhur, D.: Damage to legged wine storage tanks during the 2013 and 2016 New Zealand earthquakes. J. Constr. Steel Res. **172**, 106226 (2020b). https://doi.org/10.1016/j.jcsr.2020.106226
16. Sezen, H., Whittaker, A.S.: Seismic performance of industrial facilities affected by the 1999 Turkey earthquake. J. Perform. Constr. Facil. (ASCE) **20**(1), 28–36 (2006). https://doi.org/10.1061/(ASCE)0887-3828(2006)20:1(28)
17. Karamanos, S. A.: Sloshing effects on the seismic design of horizontal-cylindrical and spherical vessels. In: Pressure Vessels and Piping Conference, Vol. 46814, pp. 225–231. American Society of Mechanical Engineers (2004). https://doi.org/10.1115/pvp2004-2912
18. Karamanos, S.A., Patkas, L.A., Platyrrachos, M.A.: Sloshing effects on the seismic design of horizontal-cylindrical and spherical industrial vessels. J. Press. Vessel Technol. (ASME) **128**(3), 328–340 (2006). https://doi.org/10.1115/1.2217965

19. Patkas, L.A., Karamanos, S.A.: Variational solutions for externally induced sloshing in horizontal-cylindrical and spherical vessels. J. Eng. Mech. (ASCE) **133**(6), 641–655 (2007). https://doi.org/10.1061/(ASCE)0733-9399(2007)133:6(641)
20. Drosos, G.C., Dimas, A.A., Karabalis, D.L.: Discrete models for seismic analysis of liquid storage tanks of arbitrary shape and fill height. J. Press. Vessel Technol. (ASME). (2008). https://doi.org/10.1115/1.2967834
21. Vamvatsikos, D., Cornell, C.A.: Incremental dynamic analysis. Earthq. Eng. Struct. Dynam. **31**(3), 491–514 (2002). https://doi.org/10.1002/eqe.141
22. Vamvatsikos, D., Cornell, C.A.: Applied incremental dynamic analysis. Earthq. Spectra **20**(2), 523–553 (2004). https://doi.org/10.1193/1.1737737
23. Curadelli, O.: Seismic reliability of spherical containers retrofitted by means of energy dissipation devices. Eng. Struct. **33**(9), 2662–2667 (2011). https://doi.org/10.1016/j.engstruct.2011.05.015
24. Curadelli, O., Ambrosini, D.: Damage detection in elevated spherical containers partially filled with liquid. Eng. Struct. **33**(9), 2708–2715 (2011). https://doi.org/10.1016/j.engstruct.2011.05.023
25. Curadelli, O., Ambrosini, D., Mirasso, A., Amani, M.: Resonant frequencies in an elevated spherical container partially filled with water: FEM and measurement. J. Fluids Struct. **26**(1), 148–159 (2010). https://doi.org/10.1016/j.jfluidstructs.2009.10.002
26. Sivy, M., Musil, M.: Design of the spherical liquid storage tanks for earthquake resistance. Ann. Fac. Eng. Hunedoara **16**(1), 121–126 (2018)
27. Tafazoli, S., Ghazi, M., Adibnazari, S., Rofooei, F.R.: Investigating the behavior of cracks in welded zones of supporting structure of spherical pressure vessel under seismic loading. J. Constr. Steel Res. **191**, 107194 (2022). https://doi.org/10.1016/j.jcsr.2022.107194
28. Diamanti, K., Doukas, I., Karamanos, S. A.: Seismic analysis and design of industrial pressure vessels. In: III ECCOMAS Thematic Conference on Computational Methods in Structural Dynamics and Earthquake Engineering, (COMPDYN2011), Corfu, Greece (2011)
29. Uriz, P., Filippou, F.C., Mahin, S.A.: Model for cyclic inelastic buckling of steel braces. J. Struct. Eng. **134**(4), 619–628 (2008). https://doi.org/10.1061/(ASCE)0733-9445(2008)134:4(619)
30. Hsiao, P.C., Lehman, D.E., Roeder, C.W.: A model to simulate special concentrically braced frames beyond brace fracture. Earthq. Eng. Struct. Dyn. **42**(2), 183–200 (2013). https://doi.org/10.1002/eqe.2202
31. McKenna, F., and Fenves, G. L.: The OpenSees Command Language Manual (1.2 edn). Berkeley, CA: University of California Berkeley (2011). https://opensees.berkeley.edu/
32. Eurocode 8: Design of structures for earthquake resistance. Part 1: General rules, seismic actions and rules for buildings. EN1998–1. European Committee for Standardization (CEN), Brussels (2004). https://eurocodes.jrc.ec.europa.eu/showpage.php?id=138
33. Braconi A., Finetto M., Degee H., Hausoul N., Hoffmeister B., Gundel M., Karamanos S.A., Pappa P., Varelis G., Rinaldi V., Obiala R., Hjiaj M., Somja H., Badalassi M., Caprili S., Salvatore W.: Optimizing the seismic performance of steel and steel-composite concrete structures by standardizing material quality control, (OPUS) Final Report. European Commission, Directorate-General for Research and Innovation, Directorate G—Industrial Technologies, Unit G.5—Research Fund for Coal and Steel, EUR 25893 EN (2013). https://doi.org/10.2777/79330
34. Ohtsubo, H., Araki, K., Moriya, Y.: Development of SA-738 Gr. B high strength steel plate with excellent toughness for power generating plants. JFE Tech. Rep. **18**, 50–55 (2013). https://www.jfe-steel.co.jp/en/research/report/018/pdf/018-08.pdf
35. Sen, A.D., Sloat, D., Ballard, R., Johnson, M.M., Roeder, C.W., Lehman, D.E., Berman, J.W.: Experimental evaluation of the seismic vulnerability of braces and connections in older concentrically braced frames. J. Struct. Eng. (ASCE) **142**(9), 04016052 (2016). https://doi.org/10.1061/(ASCE)ST.1943-541X.0001507
36. Housner, G.W.: Dynamic pressures on accelerated fluid containers. Bull. Seismol. Soc. Am. **47**(1), 15–35 (1957). https://doi.org/10.1785/BSSA0470010015
37. Vamvatsikos, D., Cornell, C. A.: The incremental dynamic analysis and its application to performance-based earthquake engineering. In: Proceedings of the 12th European Conference on Earthquake Engineering, Vol. 40, pp. 1375–1392 (2002)
38. Jalayer, F., Cornell, C.A.: Alternative non-linear demand estimation methods for probability-based seismic assessments. Earthq. Eng. Struct. Dyn. **38**(8), 951–972 (2009). https://doi.org/10.1002/eqe.876
39. Dymiotis, C., Kappos, A.J., Chryssanthopoulos, M.K.: Seismic reliability of RC frameswith uncertain drift and member capacity. J. Struct. Eng. (ASCE) **125**(9), 1038–1047 (1999). https://doi.org/10.1061/(ASCE)0733-9445(1999)125:9(1038)
40. Kwon, O.S., Elnashai, A.: The effect of material and ground motion uncertainty on the seismic vulnerability curves of RC structure. Eng. Struct. **28**(2), 289–303 (2006). https://doi.org/10.1016/j.engstruct.2005.07.010
41. Kazantzi, A.K., Righiniotis, T.D., Chryssanthopoulos, M.K.: A simplified fragility methodology for regular steel MRFs. J. Earthq. Eng. **15**(3), 390–403 (2011). https://doi.org/10.1080/13632469.2010.498559
42. Baker, J.W.: Efficient analytical fragility function fitting using dynamic structural analysis. Earthq. Spectra **31**(1), 579–599 (2015). https://doi.org/10.1193/021113EQS025M
43. Bakalis, K., Vamvatsikos, D.: Seismic fragility functions via nonlinear response history analysis. J. Struct. Eng. (ASCE) **144**(10), 04018181 (2018). https://doi.org/10.1061/(ASCE)ST.1943-541X.0002141
44. Silva, V., Crowley, H., Varum, H., Pinho, R., Sousa, R.: Evaluation of analytical methodologies used to derive vulnerability functions. Earthq. Eng. Struct. Dyn. **43**(2), 181–204 (2014). https://doi.org/10.1002/eqe.2337
45. Silva, V., Akkar, S., Baker, J.W., Bazzurro, P., Castro, J.M., Crowley, H., Dolsek, M., Galasso, C., Lagomarsino, S., Monteiro, R., Perrone, D., Pitilakis, K., Vamvatsikos, D.: Current challenges and future trends in analytical fragility and vulnerability modelling. Earthq. Spectra **35**(4), 1927–1952 (2019). https://doi.org/10.1193/042418EQS101O
46. Cornell, C.A., Jalayer, F., Hamburger, R.O., Foutch, D.A.: The probabilistic basis for the 2000 SAC/FEMA steel moment frame guidelines. J. Struct. Eng. (ASCE) **128**(4), 526–533 (2002). https://doi.org/10.1061/(ASCE)0733-9445(2002)128:4(526)
47. Lin, T., Haselton, C.B., Baker, J.W.: Conditional spectrum-based ground motion selection Part I: hazard consistency for risk-based assessments. Earthq. Eng. Struct. Dyn. **42**(12), 1847–1865 (2013). https://doi.org/10.1002/eqe.2301

48. Kohrangi, M., Bazzurro, P., Vamvatsikos, D., Spillatura, A.: Conditional spectrum-based ground motion record selection using average spectral acceleration. Earthq. Eng. Struct. Dyn. **46**(10), 1667–1685 (2017). https://doi.org/10.1002/eqe.2876
49. Ancheta, T.D., Darragh, R.B., Stewart, J.P., et al.: NGA-West2 database. Earthq. Spectra **30**(3), 989–1005 (2014). https://doi.org/10.1193/070913EQS197M
50. Karaferis, N.D., Kazantzi, A.K., Melissianos, V.E., Bakalis, K., Vamvatsikos, D.: Seismic fragility assessment of high-rise stacks in oil refineries. Bull. Earthq. Eng. **20**(12), 6877–6900 (2022). https://doi.org/10.1007/s10518-022-01472-2
51. Bakalis, K., Kohrangi, M., Vamvatsikos, D.: Seismic intensity measures for above-ground liquid storage tanks. Earthq. Eng. Struct. Dyn. **47**(9), 1844–1863 (2018). https://doi.org/10.1002/eqe.3043
52. Luco, N., Cornell, C.A.: Structure-specific scalar intensity measures for near-source and ordinary earthquake ground motions. Earthq. Spectra **23**(2), 357–392 (2007). https://doi.org/10.1193/1.2723158
53. Kazantzi, A.K., Vamvatsikos, D.: Intensity measure selection for vulnerability studies of building classes. Earthq. Eng. Struct. Dyn. **44**(15), 2677–2694 (2015). https://doi.org/10.1002/eqe.2603
54. Weiss, N.A., et al.: A Course in Probability. Pearson Addison Wesley, Boston (2005)
55. Benjamin, J.R., Cornell, C.A.: Probability, Statistics, and Decision for Civil Engineers. Dover Publications, Mineola NY (2014)

Publisher's Note Springer Nature remains neutral with regard to jurisdictional claims in published maps and institutional affiliations.